The gravity signal of Mercury's inner core

Mathieu Dumberry[1]

[1]University of Alberta

November 26, 2022

Abstract

In a reference frame rotating with Mercury's mantle and crust, the inner core and fluid core precess in a retrograde sense with a period of 58.646 days. The precession of a triaxial inner core with a different density than the fluid core induces a periodic gravity variation of degree 2, order 1. Elastic deformations from the pressure that the precessing fluid core exerts on the core mantle boundary also contribute to this gravity signal. We show that the periodic change in Stokes coefficients ΔC21 and ΔS21 for this signal of internal origin is of the order of 10ˆ{-10}, similar in magnitude to the signal from solar tides. The relative contribution from the inner core increases with inner core radius and with the amplitude of its tilt angle with respect to the mantle. The latter depends on the strength of electromagnetic coupling at the inner core boundary which in turn depends on the radial magnetic field B_r; a larger B_r generates a larger tilt. The inner core signal features a contrast between ΔC21 and ΔS21 due to its triaxial shape, discernible for an inner core radius >500 km if B_r>0.1 mT, or for an inner core radius >1100 km if B_r<0.01 mT. A detection of this contrast would confirm the presence of an inner core and place constraints on its size and the strength of the internal magnetic field. These would provide key constraints for the thermal evolution of Mercury and for its dynamo mechanism.

The gravity signal of Mercury's inner core

Mathieu Dumberry[1]

[1]Department of Physics, University of Alberta, Edmonton, Alberta, Canada.

Key Points:

- The 58.646-day precession of Mercury's fluid and solid cores induce a periodic change in gravity coefficients C_{21} and S_{21} of $\sim 10^{-10}$
- The amplitudes of C_{21} and S_{21} depend on inner core size and radial magnetic field strength B_r inside the core
- Measuring a difference between C_{21} and S_{21} would confirm the presence of a solid inner core and constrain both its size and B_r

Corresponding author: Mathieu Dumberry, dumberry@ualberta.ca

Abstract

In a reference frame rotating with Mercury's mantle and crust, the inner core and fluid core precess in a retrograde sense with a period of 58.646 days. The precession of a triaxial inner core with a different density than the fluid core induces a periodic gravity variation of degree 2, order 1. Elastic deformations from the pressure that the precessing fluid core exerts on the core mantle boundary also contribute to this gravity signal. We show that the periodic change in Stokes coefficients ΔC_{21} and ΔS_{21} for this signal of internal origin is of the order of 10^{-10}, similar in magnitude to the signal from solar tides. The relative contribution from the inner core increases with inner core radius and with the amplitude of its tilt angle with respect to the mantle. The latter depends on the strength of electromagnetic coupling at the inner core boundary which in turn depends on the radial magnetic field B_r; a larger B_r generates a larger tilt. The inner core signal features a contrast between ΔC_{21} and ΔS_{21} due to its triaxial shape, discernible for an inner core radius $>$ 500 km if $B_r >$ 0.1 mT, or for an inner core radius $>$ 1100 km if $B_r <$ 0.01 mT. A detection of this contrast would confirm the presence of an inner core and place constraints on its size and the strength of the internal magnetic field. These would provide key constraints for the thermal evolution of Mercury and for its dynamo mechanism.

Plain language summary: Cooling over time should have led to the solidification of the central part of the fluid metallic cores in many of the rocky planets and moons of our solar system. However, we do not have firm evidence for the presence of a solid inner core in any planetary body other than Earth. In this study, we present a method that would permit a possible detection of Mercury's solid inner core. The idea exploits Mercury's rotational state: as seen by an observer on Mercury's crust, the inner core executes a retrograde precession motion at a period of 58.646 days. Since there is a density contrast at the interface between the solid and fluid core, this precession motion induces a time-dependent gravity signal. A future satellite mission that could measure the gravity field of Mercury with sufficient precision could detect this signal, and confirm the presence of a central, solid inner core. Not only would this constitute a first in our solar system, it would also provide key constraints on the thermal evolution of Mercury and on the generation of its magnetic field.

1 Introduction

Mercury's orbit normal is inclined by an angle $I = 8.5330°$ and precesses about the normal to the Laplace plane (Figure 1a) in the retrograde direction at frequency $\Omega_p = 2\pi/325,513$ yr^{-1} (Baland et al., 2017). The spin axis of Mercury is misaligned by a small obliquity angle ε_m with respect to the orbit normal. It remains coplanar with both the orbit and Laplace normals, and also precesses with frequency Ω_p. This arrangement describes a Cassini state (Colombo, 1966; Peale, 1969), and it is convenient to refer to the plane containing all three vectors as the Cassini plane.

The observed obliquity ε_m is approximately 2 arcmin (Margot et al., 2012; Stark, Oberst, Preusker, et al., 2015; Genova et al., 2019; Bertone et al., 2021) and reflects the orientation of the spin axis of the solid outer shell comprised of the mantle and crust (Figure 1b), not that of the entire planet. We know that Mercury's metallic core is partially fluid from two main lines of evidence. First, from its dynamo generated magnetic field, which must be sustained by motion in its electrically conducting core (Anderson et al., 2012; Johnson et al., 2012; Wardinski et al., 2019, 2021); and second, from the observed amplitude of its longitudinal librations, which would be smaller if the core was fully solidified (Margot et al., 2007, 2012).

Thermal evolution models of Mercury suggest that a solid inner core has most likely nucleated at its centre (Grott et al., 2011; Tosi et al., 2013; Knibbe & van Westrenen, 2018; Guerrero et al., 2021). However, if present, its size is not known. Several studies have attempted to place bounds on the inner core size, either by investigating its dynamical influence on the librations (Peale et al., 2002; Veasey & Dumberry, 2011; Dumberry, 2011; Van Hoolst et al., 2012; Dumberry et al., 2013; Yseboodt et al., 2013; Koning & Dumberry, 2013) and the mantle obliquity (Peale et al., 2016; Dumberry, 2021; MacPherson & Dumberry, 2022), or by constructing interior models that are consistent with the observed amplitude of librations and mantle obliquity (Hauck et al., 2013; Knibbe & van Westrenen, 2015; Dumberry & Rivoldini, 2015; Genova et al., 2019; Knibbe et al., 2021; Steinbrügge et al., 2021). While no general consensus has emerged from these, they all point to an inner core that cannot be too large. A limited inner core size is also favoured by numerical models of Mercury's dynamo (e.g. Christensen, 2006; Christensen & Wicht, 2008; Cao et al., 2014; Takahashi et al., 2019) and dynamical interpretations of its observed magnetic field (Wardinski et al., 2021). A large inner core ($>$ 500 km) also affects the tidal Love numbers k_2 and h_2 (Van Hoolst & Jacobs, 2003; Steinbrügge et al., 2018); a precise determination of these from observations offer then a possible path to detect the presence of an inner core.

We do not have direct observations of the orientation of the spin axis of the fluid core, nor that of the inner core. However, we expect that they should also be in a Cassini state, and their orientations should differ from that of the mantle (Peale et al., 2014, 2016; Dumberry, 2021; MacPherson & Dumberry, 2022). Their misalignment angles depend on the elliptical shapes of the core-mantle boundary (CMB) and inner core boundary (ICB) which in turn depend on the interior structure, including the size of the inner core and its density contrast with the fluid core. They also depend on the strength of viscous and electromagnetic (EM) coupling at the CMB and ICB (Peale et al., 2014, 2016; Dumberry, 2021). The dissipation associated with viscous and EM coupling also entrain a deviation of the fluid and solid cores' spin axes away from the Cassini plane (MacPherson & Dumberry, 2022).

As seen in a frame attached with the mantle and crust rotating at sidereal frequency $\Omega_o = 2\pi/58.646$ day^{-1}, the longitudinal orientation of the Cassini plane is rotating at a frequency equal to $-\Omega_o - \Omega_p \cos I$, with the negative sign indicating that the direction of this rotation is retrograde (westward). This means that for an observer in the mantle frame, the tilted axes of the fluid and inner cores execute a retrograde precession at the same frequency (Figure 1b). Because $\Omega_p/\Omega_o = 4.9327 \times 10^{-7}$, this frequency is essentially equal to $-\Omega_o$, identical to the sidereal frequency of Mercury's rotation.

The inner core, if present, has a triaxial shape and its density differs from that of the fluid core. As seen from the mantle frame, a precessing inner core generates a periodic degree 2, order 1 gravity variation, the amplitude of which depends on the size and tilt angle of the inner core and on the density contrast at the ICB. Likewise, the time variable pressure on the CMB associated with the precessing spin axis of the fluid core results in periodic global elastic deformations, also contributing to a temporal degree 2, order 1 gravity variation. If it can be de-

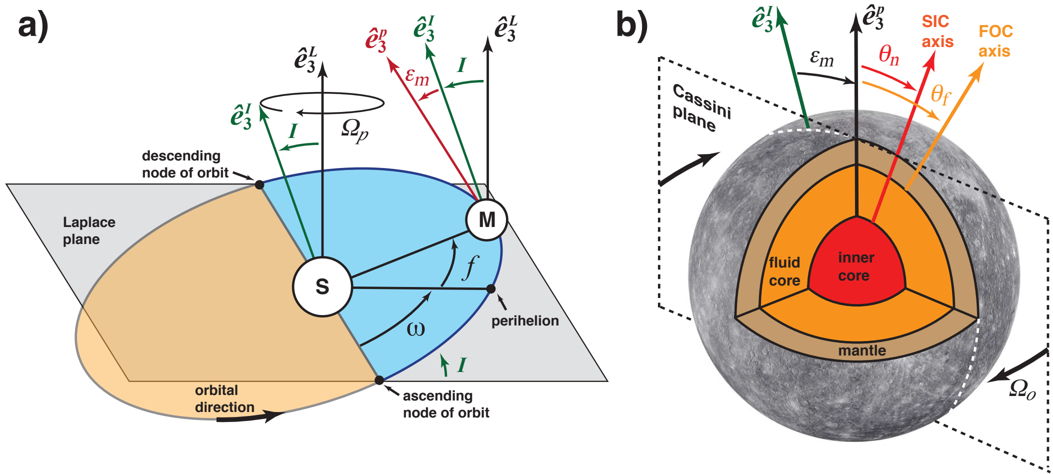

Figure 1. (a) The orbit of Mercury (M) around Sun (S) with respect to the Laplace plane (grey shaded rectangle). The normal to the orbital plane ($\hat{\mathbf{e}}_3^{\mathbf{I}}$) is offset from the normal to the Laplace plane ($\hat{\mathbf{e}}_3^{\mathbf{L}}$) by an inclination angle $I = 8.5330°$. The symmetry axis of the mantle and crust $\hat{\mathbf{e}}_3^{\mathbf{P}}$ is offset from $\hat{\mathbf{e}}_3^{\mathbf{I}}$ by $\varepsilon_m \approx 2$ arcmin. (The spin axis is misaligned from $\hat{\mathbf{e}}_3^{\mathbf{P}}$ by a small angle of 0.015 arcsec; it can be assumed aligned with $\hat{\mathbf{e}}_3^{\mathbf{P}}$ for the purpose of illustrating the geometry of the Cassini state.) $\hat{\mathbf{e}}_3^{\mathbf{I}}$ and $\hat{\mathbf{e}}_3^{\mathbf{P}}$ are coplanar with, and precess about, $\hat{\mathbf{e}}_3^{\mathbf{L}}$ in a retrograde direction at frequency $\Omega_p = 2\pi/325,513\ \mathrm{yr}^{-1}$. The blue (orange) shaded region indicates the portion of the orbit when Mercury is above (below) the Laplace plane. ω is the argument of perihelion. f is the true anomaly. (b) The Cassini state of Mercury as seen in a frame attached to the mantle and crust rotating at sidereal frequency $\Omega_o = 2\pi/58.646\ \mathrm{day}^{-1}$. The spin axis of the fluid outer core (FOC, orange) and the figure axis of the solid inner core (SIC, red) are misaligned respectively by angles θ_f and θ_n from the mantle axis. Viscous and EM coupling at the ICB and CMB lead to a deviation of the spin axes of the FOC and SIC with respect to the Cassini plane; they are depicted here as lying in the Cassini plane only for ease of illustration. For an observer on the mantle, the Cassini plane is rotating westward at frequency Ω_o around $\hat{\mathbf{e}}_3^{\mathbf{P}}$ so the tilted FOC and SIC axes execute a retrograde precession at the same frequency. Angles in both panels are not drawn to scale.

tected, this gravity variation of internal origin offers then an opportunity to constrain Mercury's interior structure, including wether a solid inner core is present at its centre.

The objective of our study is to present plausible predictions of the amplitude of this internal gravity signal in order to establish the observational precision that would be required to detect it. To do so, we use the rotational model of the Cassini state of Mercury presented in Dumberry (2021) and further developed in MacPherson and Dumberry (2022), which are henceforth referred to as D21 and MD22, respectively. The presence and size of an inner core is an important diagnostic of the thermal evolution of a planetary body. Even though we expect that the central part of the metallic cores of many planets and moons is solid, just as it is for Earth, we do not have any firm evidence to confirm this. A detection of Mercury's inner core through its gravity signal would then add a key constraint on the formation and evolution of terrestrial-like planetary bodies.

An analogous idea has been proposed for the Moon (Williams, 2007). The Moon is also in a Cassini state and the frequency of one its free rotational mode, the free inner core nutation (FICN), is close to its precession frequency of $2\pi/18.6$ yr^{-1}. A large inner core tilt can thus result by resonant amplification of the FICN mode (Williams, 2007; Dumberry & Wieczorek, 2016; Stys & Dumberry, 2018). Hence, although the core of the Moon is small, and its inner core even smaller, the predicted periodic change in the Stokes coefficients of degree 2, order 1 can nevertheless be of the order of 10^{-10} (Williams, 2007; Zhang & Dumberry, 2021). One objective of the GRAIL satellite mission (e.g. Zuber et al., 2013) was to detect this gravity signal, although a clear signal has yet to emerge from the data (Williams et al., 2015).

In contrast with the Moon, the FICN frequency of Mercury is far from the precession frequency Ω_p, so the predicted inner core tilt angle is much smaller (Peale et al., 2016, D21). Nevertheless, because Mercury's fluid core is very large, and its inner core also potentially large, their precession can produce a sizeable gravity signal, as we show below. Furthermore, as we also show, this internal gravity signal is of the same order as the degree 2, order 1 signal from solar tides, increasing the likelihood that it can be extracted from observations.

2 The gravity signal associated with the precession of Mercury

2.1 Definition of the reference frames and angles of tilt

We define a frame of reference centred on Mercury and attached to the solid outer shell comprised of the crust and mantle, with unit vectors $(\mathbf{\hat{e}_1^p}, \mathbf{\hat{e}_2^p}, \mathbf{\hat{e}_3^p})$ aligned with the direction of the principal moments of inertia (A, B, C) of the whole planet. We also define a spherical coordinate system (r, ϑ, φ) with radius r, colatitude ϑ and longitude φ, with coordinates ($\vartheta = 0$), ($\vartheta = \frac{\pi}{2}$, $\varphi = 0$) and ($\vartheta = \frac{\pi}{2}$, $\varphi = \frac{\pi}{2}$) coinciding respectively with the axes of C, A and B.

Because of Mercury's Cassini state, $\mathbf{\hat{e}_3^p}$ is offset from the orbit normal $\mathbf{\hat{e}_3^I}$ by an obliquity angle ε_m (Figure 1). If we neglect small longitudinal librations, when Mercury is at perihelion, the projection of the long equatorial axis $\mathbf{\hat{e}_1^p}$ onto the orbital plane is aligned with the Mercury-Sun line. Mercury is in a 3:2 spin-orbit resonance, in which the sidereal rotation frequency Ω_o is 1.5 times the mean motion n (or, equivalently, the orbital frequency). As a result, the hemisphere that faces the Sun alternate with each passage of perihelion. We set the reference time $t = 0$ to correspond to when $\mathbf{\hat{e}_1^p}$ is pointing toward the Sun.

To track the orientation of the inner core with respect to the mantle, we also define a frame attached to the inner core by unit vectors $(\hat{\mathbf{e}}_{\mathbf{1}}^{\mathbf{s}}, \hat{\mathbf{e}}_{\mathbf{2}}^{\mathbf{s}}, \hat{\mathbf{e}}_{\mathbf{3}}^{\mathbf{s}})$ aligned with the direction of the principal moments of inertia (A_s, B_s, C_s). The triaxial shape of the inner core is specified such that it is aligned with that of the whole planet when averaged over one orbit, $(\hat{\mathbf{e}}_{\mathbf{1}}^{\mathbf{s}}, \hat{\mathbf{e}}_{\mathbf{2}}^{\mathbf{s}}, \hat{\mathbf{e}}_{\mathbf{3}}^{\mathbf{s}}) = (\hat{\mathbf{e}}_{\mathbf{1}}^{\mathbf{p}}, \hat{\mathbf{e}}_{\mathbf{2}}^{\mathbf{p}}, \hat{\mathbf{e}}_{\mathbf{3}}^{\mathbf{p}})$. Because of the differential precession of the inner core, this alignment does not apply at any specific time snapshot. Note that the tilted inner core causes a small misalignment of the principal moments of inertia of the whole planet with respect to $(\hat{\mathbf{e}}_{\mathbf{1}}^{\mathbf{p}}, \hat{\mathbf{e}}_{\mathbf{2}}^{\mathbf{p}}, \hat{\mathbf{e}}_{\mathbf{3}}^{\mathbf{p}})$, though this offset does not exceed 0.01 arcmin (D21).

We must define several additional angles to complete the description of Mercury's Cassini state. The outer shell comprised of the mantle and crust form a single rotating region; we refer to this shell as the 'mantle' when describing Mercury's rotation dynamics. We denote the rotation rate vector of the mantle as $\mathbf{\Omega}$. In the Cassini state, $\mathbf{\Omega}$ does not coincide with the symmetry axis $\hat{\mathbf{e}}_{\mathbf{3}}^{\mathbf{p}}$; their misalignment is defined by an angle θ_m. However, $\theta_m \approx 0.015$ arcsec (D21); even though the orientations of the spin and figure axes of the mantle are both retained in our rotational model, they can be considered coincident in the Cassini state. Three additional angles must be defined to describe the Cassini state of the fluid and solid cores. We define the misalignment between the symmetry axes of the inner core $\hat{\mathbf{e}}_{\mathbf{3}}^{\mathbf{s}}$ and mantle $\hat{\mathbf{e}}_{\mathbf{3}}^{\mathbf{p}}$ by an angle θ_n. The rotation vectors of the fluid core and inner core are denoted by $\mathbf{\Omega_f}$ and $\mathbf{\Omega_s}$, respectively, and their misalignment from $\mathbf{\Omega}$ are defined by angles θ_f and θ_s. A graphical representation of all these angles is shown in Figure 2 of D21. Note that the rotation and symmetry axes of the inner core remain in close alignment in the Cassini state; for a tilt of the inner core figure of $\theta_n =$ 1 arcmin with respect to the mantle, θ_s is offset from θ_n by approximately 0.03 milliarcsec (MD22). Although we keep track of both θ_n and θ_s in our rotational model, to a very good approximation, $\theta_n = \theta_s$.

Tidal dissipation introduces a misalignment of $\hat{\mathbf{e}}_{\mathbf{3}}^{\mathbf{p}}$ (and $\mathbf{\Omega}$) with respect to the Cassini plane. For a tidal quality factor Q of approximately 100 or larger, $\hat{\mathbf{e}}_{\mathbf{3}}^{\mathbf{p}}$ lags behind the Cassini plane by an angle smaller than 1 arcsec (Baland et al., 2017, MD22). Observations of the orientation of the spin axis of Mercury suggest that the deviation is limited to at most a few arcsec (e.g. Margot et al., 2012; Stark, Oberst, Preusker, et al., 2015; Genova et al., 2019; Bertone et al., 2021). With respect to the orientation of the Cassini plane, a deviation of 1 arcsec corresponds to a longitudinal offset angle of $\phi_m = \tan^{-1}(1 \text{ arcsec} / 2 \text{ arcmin}) \approx 0.5°$. For simplicity, we neglect this small misalignment and assume that $\hat{\mathbf{e}}_{\mathbf{3}}^{\mathbf{p}}$ is aligned with the Cassini plane.

Viscous and EM dissipation at the ICB and CMB induce an additional deviation of $\hat{\mathbf{e}}_{\mathbf{3}}^{\mathbf{p}}$ away from the Cassini plane, but by no more than 0.1 arcsec (MD22). Although their effect on the orientation of $\hat{\mathbf{e}}_{\mathbf{3}}^{\mathbf{p}}$ can be neglected, viscous and EM coupling result in deviations of the spin axis of the fluid core and figure axis of the inner core from the Cassini plane that are of the order of a few tens of arcsec, similar in amplitude to their tilt components in the Cassini plane. We denote by ϕ_f and ϕ_n the longitudinal orientations of the spin axis of the fluid core and figure axis of the inner core with respect to the Cassini plane.

2.2 Gravity variations of degree 2, order 1 from solar tides

The tide generating potential (TGP) V_t of harmonic degree 2 at a geographic location (ϑ, φ) at the surface of Mercury (radius $r = R$) due to the Sun (mass $M_\odot = 1.9891 \times 10^{30}$ kg) located at a radial distance d, colatitude ϑ_s and longitude φ_s is given by (e.g. Equations 4.7 and 4.16 of Murray & Dermott, 1999)

$$V_t(r,\vartheta,\varphi) = -\frac{GM_\odot}{d}\left(\frac{R}{d}\right)^2 \Big[P_{20}(\cos\vartheta)P_{20}(\cos\vartheta_s) + \frac{1}{3}P_{21}(\cos\vartheta)P_{21}(\cos\vartheta_s)\cos(\varphi-\varphi_s) + \frac{1}{12}P_{22}(\cos\vartheta)P_{22}(\cos\vartheta_s)\cos(2\varphi-2\varphi_s)\Big]\,, \tag{1}$$

where G is the gravitational constant and

$$P_{20}(\cos\vartheta) = \frac{1}{2}(3\cos^2\vartheta - 1)\,, \qquad P_{21}(\cos\vartheta) = 3\sin\vartheta\cos\vartheta\,, \qquad P_{22}(\cos\vartheta) = 3\sin^2\vartheta\,, \tag{2}$$

are the unnormalized associated Legendre polynomials of degree 2. The TGP induces a tidal deformation of Mercury which produces an additional gravitational potential. The total gravitational potential can be expressed as

$$V = V_t(1+k_2)\,, \tag{3}$$

where k_2 is the degree 2 Love number.

The gravitational potential at a position (r,ϑ,φ) above Mercury's surface can also be expressed in terms of a spherical harmonic expansion as

$$V(r,\vartheta,\varphi) = -\frac{GM_☿}{r}\left(1+\sum_{lm}\left(\frac{R}{r}\right)^l (C_{lm}\cos m\varphi + S_{lm}\sin m\varphi)\,P_{lm}(\cos\vartheta)\right)\,, \tag{4}$$

where $M_☿ = 3.3041 \times 10^{23}$ kg is Mercury's mass and C_{lm} and S_{lm} are the (unnormalized) Stokes coefficients of degree l and order m. Static, non-spherical mass anomalies constitute the dominant part of C_{lm} and S_{lm}, but the TGP and the precession associated with the Cassini state induce time-dependent variations at degree 2. By equating the potential at $r = R$ from Equation (4) with that of Equation (3), the time-dependent Stokes coefficients of degree 2 (denoted by $\Delta C^{ext}_{2m}(t)$, $\Delta S^{ext}_{2m}(t)$) caused by solar tides are

$$\Delta C^{ext}_{20}(t) = (1+k_2)\mathcal{C}P_{20}(\cos\vartheta_s)\,, \tag{5a}$$

$$\Delta C^{ext}_{21}(t) = (1+k_2)\frac{\mathcal{C}}{3}P_{21}(\cos\vartheta_s)\cos\varphi_s\,, \qquad \Delta S^{ext}_{21}(t) = (1+k_2)\frac{\mathcal{C}}{3}P_{21}(\cos\vartheta_s)\sin\varphi_s\,, \tag{5b}$$

$$\Delta C^{ext}_{22}(t) = (1+k_2)\frac{\mathcal{C}}{12}P_{22}(\cos\vartheta_s)\cos 2\varphi_s\,, \qquad \Delta S^{ext}_{22}(t) = (1+k_2)\frac{\mathcal{C}}{12}P_{22}(\cos\vartheta_s)\sin 2\varphi_s\,, \tag{5c}$$

where

$$\mathcal{C} = \frac{M_\odot}{M_☿}\left(\frac{R}{d}\right)^3\,. \tag{6}$$

The position of the Sun $(d,\ \vartheta_s,\ \varphi_s)$ as seen in Mercury's frame is time-dependent. With the choice of $t = 0$ corresponding to when Mercury is at perihelion with $\hat{\mathbf{e}}_1$ pointing toward the Sun, the temporally varying colatitude position of the Sun can be written as $\vartheta_s(t) = \pi/2 - \varepsilon_m(t)$, where $\varepsilon_m(t)$ is its temporally varying latitude, connected to the obliquity ε_m by

$$\varepsilon_m(t) = \varepsilon_m \sin(f + \omega)\,, \tag{7}$$

where f is the true anomaly and ω is the argument of perihelion taken to be 50.3796° (Baland et al., 2017). If Mercury were not rotating, the longitudinal position of the Sun would be simply $\varphi_s(t) = f$. As seen in Mercury's frame rotating at frequency Ω_o, we thus have

$$\varphi_s(t) = -\Omega_o t + f = -\frac{3}{2}M + f\,, \tag{8}$$

where $M = nt$ is the mean anomaly and where we have used $\Omega_o = \frac{3}{2}n$.

As we show in the next two sections, the gravity signal caused by the precession of the inner core and fluid core cause a periodic degree 2 gravity signal dominantly at order 1, so we focus on the tidal gravity signal of order 1. Because ε_m is very small, we can use the approximation

$$P_{21}(\cos\vartheta_s) = 3\cos\vartheta_s \sin\vartheta_s = \frac{3}{2}\sin 2\vartheta_s = \frac{3}{2}\sin(2\varepsilon_m(t)) \approx 3\,\varepsilon_m(t)\,, \tag{9}$$

so the time variation of the degree 2, order 1 Stokes coefficients are given by

$$\Delta C_{21}^{ext}(t) = (1 + k_2)\,\mathcal{C}\,\varepsilon_m \sin(f + \omega)\cos\left(-\frac{3}{2}M + f\right)\,, \tag{10a}$$

$$\Delta S_{21}^{ext}(t) = (1 + k_2)\,\mathcal{C}\,\varepsilon_m \sin(f + \omega)\sin\left(-\frac{3}{2}M + f\right)\,. \tag{10b}$$

Mercury's orbit is elliptical, with an eccentricity $e_c = 0.20563$, and expanded to third order in e_c, the true anomaly f and distance d are related to the mean anomaly M and semi-major axis $a = 57.91 \times 10^6$ km by (e.g. Murray & Dermott, 1999)

$$f = M + 2e_c \sin M + \frac{5}{4}e_c^2 \sin 2M + e_c^3\left(\frac{13}{12}\sin 3M - \frac{1}{4}\sin M\right)\,, \tag{11a}$$

$$d = a\left[1 - e_c \cos M + e_c^2(1 - \cos 2M) + \frac{3}{8}e_c^3\,(\cos M - \cos 3M)\right]\,. \tag{11b}$$

If Mercury's orbit were circular ($e_c = 0$), then $f = M = nt$, $d = a$ and the predictions of $\Delta C_{21}^{ext}(t)$ and $\Delta S_{21}^{ext}(t)$ from Equation (10) would be given by

$$\Delta C_{21}^{ext}(t) = \frac{1}{2}(1 + k_2)\,\mathcal{C}_a\,\varepsilon_m\left[\sin\left(\frac{3nt}{2} + \omega\right) + \sin\left(\frac{nt}{2} + \omega\right)\right]\,, \tag{12a}$$

$$\Delta S_{21}^{ext}(t) = \frac{1}{2}(1 + k_2)\,\mathcal{C}_a\,\varepsilon_m\left[\cos\left(\frac{3nt}{2} + \omega\right) - \cos\left(\frac{nt}{2} + \omega\right)\right]\,, \tag{12b}$$

with the constant $\mathcal{C}_a$ given by Equation (6) but with $d = a$. The solar tide gravity signal would then be comprised of a sum of two frequencies: a retrograde signal of frequency $\frac{3}{2}n = \Omega_o$, and a prograde signal of frequency $\frac{1}{2}n = \frac{1}{3}\Omega_o$. The eccentricity of Mercury's orbit introduces additional periodicities, but these two frequencies dominate the degree 2, order 1 solar tide signal (Van Hoolst & Jacobs, 2003).

Anelastic deformations results in an out-of-phase gravity signal (delayed by a quarter of a cycle) with an amplitude smaller by the tidal quality factor Q than that associated with elastic deformations (e.g. Baland et al., 2017). Q is unknown for Mercury, but should be of the order of 100 or larger for a bulk mantle viscosity larger than 10^{18} Pa s (MD22), so we neglect the small contribution to $\Delta C_{21}^{ext}(t)$ and $\Delta C_{21}^{ext}(t)$ from anelastic tidal deformations. This is consistent with our choice to neglect the small longitudinal offset of the mantle figure from the Cassini plane induced by tidal dissipation.

2.3 The gravity signal of a precessing inner core

The moment of inertia tensor of the (rigid) inner core is defined as

$$\boldsymbol{\mathcal{I}_s} = A_s \hat{\mathbf{e}}^{\mathbf{s}}_{\mathbf{1}} \hat{\mathbf{e}}^{\mathbf{s}}_{\mathbf{1}} + B_s \hat{\mathbf{e}}^{\mathbf{s}}_{\mathbf{2}} \hat{\mathbf{e}}^{\mathbf{s}}_{\mathbf{2}} + C_s \hat{\mathbf{e}}^{\mathbf{s}}_{\mathbf{3}} \hat{\mathbf{e}}^{\mathbf{s}}_{\mathbf{3}} \,. \tag{13}$$

Because the inner core is precessing about $\hat{\mathbf{e}}^{\mathbf{p}}_{\mathbf{3}}$, when expressed in the mantle frame, $\boldsymbol{\mathcal{I}_s}$ is time-dependent, it has off-diagonal elements, and its diagonal elements are no longer as simple as those given by Equation (13). With our expansion of the gravitational potential in terms of unnormalized associated Legendre polynomials in Equation (4), the degree 2 Stokes coefficients associated with the precession of the inner core (denoted by $\Delta C^n_{2m}(t)$, $\Delta S^n_{2m}(t)$) are connected to the elements of $\boldsymbol{\mathcal{I}_s}$ by,

$$\begin{aligned}
\Delta C^n_{20}(t) &= -\frac{\alpha_3 \Big((\boldsymbol{\mathcal{I}_s})_{33} - \frac{1}{2}((\boldsymbol{\mathcal{I}_s})_{11} + (\boldsymbol{\mathcal{I}_s})_{22}) \Big)}{M_☿ R^2} \,, \\
\Delta C^n_{21}(t) &= -\frac{\alpha_3 (\boldsymbol{\mathcal{I}_s})_{13}}{M_☿ R^2} \,, & \Delta S^n_{21}(t) &= -\frac{\alpha_3 (\boldsymbol{\mathcal{I}_s})_{23}}{M_☿ R^2} \,, \\
\Delta C^n_{22}(t) &= \frac{\alpha_3 \Big((\boldsymbol{\mathcal{I}_s})_{22} - (\boldsymbol{\mathcal{I}_s})_{11} \Big)}{4 M_☿ R^2} \,, & \Delta S^n_{22}(t) &= -\frac{\alpha_3 (\boldsymbol{\mathcal{I}_s})_{12}}{2 M_☿ R^2} \,,
\end{aligned} \tag{14}$$

where $\alpha_3 = 1 - \rho_f/\rho_s$ is the density contrast between the fluid core (ρ_f) and inner core (ρ_s) at the ICB. To determine the time-dependency of the elements of $\boldsymbol{\mathcal{I}_s}$, we must express how the coordinate system $(\hat{\mathbf{e}}^{\mathbf{s}}_{\mathbf{1}}, \hat{\mathbf{e}}^{\mathbf{s}}_{\mathbf{2}}, \hat{\mathbf{e}}^{\mathbf{s}}_{\mathbf{3}})$ of a precessing inner core changes as a function of time in the mantle frame ($\hat{\mathbf{e}}^{\mathbf{p}}$−frame).

A rotation by an angle θ of the coordinate system $(\hat{\mathbf{e}}^{\mathbf{s}}_{\mathbf{1}}, \hat{\mathbf{e}}^{\mathbf{s}}_{\mathbf{2}}, \hat{\mathbf{e}}^{\mathbf{s}}_{\mathbf{3}})$ in a direction $\hat{\mathbf{k}} = (k_1, k_2, k_3)$, defined in the $\hat{\mathbf{e}}^{\mathbf{p}}$−frame, can be written in terms of a general rotation matrix $\boldsymbol{\mathcal{R}}(\hat{\mathbf{k}}, \theta)$,

$$\boldsymbol{\mathcal{R}}(\hat{\mathbf{k}}, \theta) = \begin{bmatrix} \cos\theta + k_1^2(1-\cos\theta) & k_1 k_2 (1-\cos\theta) - k_3 \sin\theta & k_1 k_3 (1-\cos\theta) + k_2 \sin\theta \\ k_1 k_2 (1-\cos\theta) + k_3 \sin\theta & \cos\theta + k_2^2(1-\cos\theta) & k_2 k_3 (1-\cos\theta) - k_1 \sin\theta \\ k_1 k_3 (1-\cos\theta) - k_2 \sin\theta & k_2 k_3 (1-\cos\theta) + k_1 \sin\theta & \cos\theta + k_3^2(1-\cos\theta) \end{bmatrix} . \tag{15}$$

If we define φ_n as the instantaneous longitudinal direction of the tilt of $\hat{\mathbf{e}}^{\mathbf{s}}_{\mathbf{3}}$ as seen in the $\hat{\mathbf{e}}^{\mathbf{p}}$-frame, then

$$\hat{\mathbf{k}} = -\sin\varphi_n \hat{\mathbf{e}}_\mathbf{1} + \cos\varphi_n \hat{\mathbf{e}}_\mathbf{2} \,. \tag{16}$$

For a tilt of the inner core figure by an angle θ_n toward a longitudinal direction φ_n, the orientation of the principal axes of the inner core as seen in the mantle frame are

$$\begin{aligned}
\hat{\mathbf{e}}^{\mathbf{s}}_\mathbf{1} &= \boldsymbol{\mathcal{R}}(\hat{\mathbf{k}},\theta_n)\cdot\hat{\mathbf{e}}_\mathbf{1} && \text{(17a)}\\
&= \Big[\cos\theta_n + \sin^2\varphi_n\big(1-\cos\theta_n\big)\Big]\hat{\mathbf{e}}_\mathbf{1} - \cos\varphi_n\sin\varphi_n\big(1-\cos\theta_n\big)\hat{\mathbf{e}}_\mathbf{2} - \cos\varphi_n\sin\theta_n\,\hat{\mathbf{e}}_\mathbf{3}\,, \\
\hat{\mathbf{e}}^{\mathbf{s}}_\mathbf{2} &= \boldsymbol{\mathcal{R}}(\hat{\mathbf{k}},\theta_n)\cdot\hat{\mathbf{e}}_\mathbf{2} && \text{(17b)}\\
&= -\cos\varphi_n\sin\varphi_n\big(1-\cos\theta_n\big)\hat{\mathbf{e}}_\mathbf{1} + \Big[\cos\theta_n + \cos^2\varphi_n\big(1-\cos\theta_n\big)\Big]\hat{\mathbf{e}}_\mathbf{2} - \sin\varphi_n\sin\theta_n\,\hat{\mathbf{e}}_\mathbf{3}\,, \\
\hat{\mathbf{e}}^{\mathbf{s}}_\mathbf{3} &= \boldsymbol{\mathcal{R}}(\hat{\mathbf{k}},\theta_n)\cdot\hat{\mathbf{e}}_\mathbf{3} && \text{(17c)}\\
&= \cos\varphi_n\sin\theta_n\,\hat{\mathbf{e}}_\mathbf{1} + \sin\varphi_n\sin\theta_n\,\hat{\mathbf{e}}_\mathbf{2} + \cos\theta_n\,\hat{\mathbf{e}}_\mathbf{3}\,.
\end{aligned}$$

Substituting these into Equation (13), the elements of the symmetric moment of inertial tensor $\boldsymbol{\mathcal{I}_s}$ are thus,

$$(\boldsymbol{\mathcal{I}_s})_{11} = A_s\big(\cos\theta_n\cos^2\varphi_n + \sin^2\varphi_n\big)^2 + B_s\big(1-\cos\theta_n\big)^2\sin^2\varphi_n\cos^2\varphi_n + C_s\sin^2\theta_n\cos^2\varphi_n \tag{18a}$$

$$(\boldsymbol{\mathcal{I}_s})_{22} = A_s\big(1-\cos\theta_n\big)^2\sin^2\varphi_n\cos^2\varphi_n + B_s\big(\cos\theta_n\sin^2\varphi_n + \cos^2\varphi_n\big)^2 + C_s\sin^2\theta_n\sin^2\varphi_n \tag{18b}$$

$$(\boldsymbol{\mathcal{I}_s})_{33} = A_s\sin^2\theta_n\cos^2\varphi_n + B_s\sin^2\theta_n\sin^2\varphi_n + C_s\cos^2\theta_n \tag{18c}$$

$$\begin{aligned}(\boldsymbol{\mathcal{I}_s})_{12} = \Big[&-A_s(1-\cos\theta_n)\big(\cos\theta_n\cos^2\varphi_n + \sin^2\varphi_n\big)\\
&- B_s(1-\cos\theta_n)\big(\cos\theta_n\sin^2\varphi_n + \cos^2\varphi_n\big) + C_s\sin^2\theta_n\Big]\sin\varphi_n\cos\varphi_n\end{aligned} \tag{18d}$$

$$(\boldsymbol{\mathcal{I}_s})_{13} = \Big[(C_s-A_s)\cos\theta_n + (B_s-A_s)(1-\cos\theta_n)\sin^2\varphi_n\Big]\sin\theta_n\cos\varphi_n \tag{18e}$$

$$(\boldsymbol{\mathcal{I}_s})_{23} = \Big[(C_s-B_s)\cos\theta_n - (B_s-A_s)(1-\cos\theta_n)\cos^2\varphi_n\Big]\sin\theta_n\sin\varphi_n \tag{18f}$$

As seen in the mantle frame, θ_n remains constant in time (a discussion on this point is presented further ahead in section 3.2). The longitudinal direction φ_n is fixed with respect to the Cassini plane, but the Cassini plane itself is rotating in the retrograde direction at frequency Ω_o with respect to the mantle (Figure 1b). Hence, φ_n is time-dependent, and to make this explicit, we write it as $\varphi_n(t)$ (the definition of $\varphi_n(t)$ is given further below). Because θ_n is small, of the order of a few arcmin or smaller, terms proportional to $\sin^2\theta_n$ and $(1-\cos\theta_n)$ are very small, and the leading order time-dependent components of $\boldsymbol{\mathcal{I}_s}$ are $(\boldsymbol{\mathcal{I}_s})_{13}$ and $(\boldsymbol{\mathcal{I}_s})_{23}$. Hence, the Stokes coefficients of degree 2 that feature the largest time-dependent changes are $\Delta C^n_{21}(t)$ and $\Delta S^n_{21}(t)$ (see Equation 14). With the approximation $\cos\theta_n \approx 1$, they are given by

$$\Delta C^n_{21}(t) = -\Delta C^{n,rig}_{21}\cos\big(\varphi_n(t)\big)\,, \tag{19a}$$

$$\Delta S^n_{21}(t) = -\Delta S^{n,rig}_{21}\sin\big(\varphi_n(t)\big)\,, \tag{19b}$$

where the magnitudes $\Delta C_{21}^{n,rig}$ and $\Delta S_{21}^{n,rig}$ are given by

$$\Delta C_{21}^{n,rig} = \alpha_3 \frac{(C_s - A_s)}{M_☿ R^2} \sin\theta_n \,, \tag{20a}$$

$$\Delta S_{21}^{n,rig} = \alpha_3 \frac{(C_s - B_s)}{M_☿ R^2} \sin\theta_n \,. \tag{20b}$$

Equations (19) and (20) capture the leading order gravity signal associated with a precessing, rigid inner core. The global change in gravitational potential leads to global elastic deformations, and this creates an additional contribution to the gravity signal. If we denote the magnitude of this contribution (in terms of Stokes coefficients) by $\Delta C_{21}^{n,def}$ and $\Delta S_{21}^{n,def}$, they are connected to $\Delta C_{21}^{n,rig}$ and $\Delta S_{21}^{n,rig}$ by a Love number k_s (see Equation C.4 of MD22),

$$\Delta C_{21}^{n,def} = k_s \, \Delta C_{21}^{n,rig} \,, \tag{21a}$$

$$\Delta S_{21}^{n,def} = k_s \, \Delta S_{21}^{n,rig} \,, \tag{21b}$$

so that

$$\Delta C_{21}^{n}(t) = -\left(\Delta C_{21}^{n,rig} + \Delta C_{21}^{n,def}\right) \cos\left(\varphi_n(t)\right) = -\Delta C_{21}^{n,rig}(1+k_s)\cos\left(\varphi_n(t)\right) \,, \tag{22a}$$

$$\Delta S_{21}^{n}(t) = -\left(\Delta S_{21}^{n,rig} + \Delta S_{21}^{n,def}\right) \sin\left(\varphi_n(t)\right) = -\Delta S_{21}^{n,rig}(1+k_s)\sin\left(\varphi_n(t)\right) \,. \tag{22b}$$

The remaining task is to express the longitude direction $\varphi_n(t)$ as a function of time. As mentioned above, the retrograde precession of the inner core as seen in the mantle frame implies a time-dependent part of $\varphi_n(t)$ equal to $-\Omega_o t$. With our choice of origin time at perihelion with $\hat{\mathbf{e}}_\mathbf{1}^\mathbf{P}$ pointing to the Sun, the longitudinal orientation of the Cassini plane at $t = 0$ is $\frac{\pi}{2} - \omega$. Because of viscous and EM dissipation, the inner core tilt deviates from the Cassini plane by a longitudinal angle ϕ_n. Therefore, we can write

$$\varphi_n(t) = -\Omega_o t + \frac{\pi}{2} - \omega + \phi_n \,, \tag{23}$$

so that

$$\Delta C_{21}^{n}(t) = -\Delta C_{21}^{n,rig}(1+k_s)\cos\left(-\Omega_o t + \frac{\pi}{2} - \omega + \phi_n\right) \,, \tag{24a}$$

$$\Delta S_{21}^{n}(t) = -\Delta S_{21}^{n,rig}(1+k_s)\sin\left(-\Omega_o t + \frac{\pi}{2} - \omega + \phi_n\right) \,. \tag{24b}$$

Anelastic deformations within the inner core and mantle in response to a tilted inner core also contribute to the gravity signal. We assume here that these are small, and we neglect their contributions.

2.4 The gravity signal from the misaligned rotation vectors

As seen from the mantle frame, the mantle rotation vector $\mathbf{\Omega}$ traces a retrograde precession with angle θ_m about $\hat{\mathbf{e}}_\mathbf{3}^\mathbf{P}$. This periodic change in the centrifugal potential induces elastic deformations which contribute to the gravity signal of internal origin. If the rotation vectors of the fluid and solid cores are aligned with that of the mantle $\mathbf{\Omega}$, the perturbation in the moment of inertia tensor of the whole planet induced by $\mathbf{\Omega}$ is

$$\Delta\boldsymbol{\mathcal{I}} = \frac{k_2 R^5}{3G}\left(\mathbf{\Omega}\mathbf{\Omega} - \frac{1}{3}|\mathbf{\Omega}|^2\mathbf{I}\right), \tag{25}$$

where $\mathbf{I}$ is the identity matrix. The misalignment of the rotation vectors of the fluid and solid cores with respect to $\mathbf{\Omega}$ causes additional deformations which are treated separately below. Writing $\mathbf{\Omega} = \Omega_o \hat{\mathbf{e}}_\mathbf{3}^\mathbf{\Omega}$, the direction $\hat{\mathbf{e}}_\mathbf{3}^\mathbf{\Omega}$ in the mantle frame depends on the (fixed) tilt angle θ_m and the (time-dependent) longitudinal orientation φ_m,

$$\hat{\mathbf{e}}_\mathbf{3}^\mathbf{\Omega} = \sin\theta_m\left(\cos\varphi_m\,\hat{\mathbf{e}}_\mathbf{1}^\mathbf{P} + \sin\varphi_m\,\hat{\mathbf{e}}_\mathbf{2}^\mathbf{P}\right) + \cos\theta_m\,\hat{\mathbf{e}}_\mathbf{3}^\mathbf{P}\,. \tag{26}$$

The perturbation in the moment of inertia tensor is then

$$\Delta\boldsymbol{\mathcal{I}} = \frac{k_2 R^5 \Omega_o^2}{3G}\left(\hat{\mathbf{e}}_\mathbf{3}^\mathbf{\Omega}\hat{\mathbf{e}}_\mathbf{3}^\mathbf{\Omega} - \frac{1}{3}\mathbf{I}\right), \tag{27}$$

and its symmetric elements in the $\hat{\mathbf{e}}^\mathbf{P}$-frame can be constructed from Equation (26). The leading order time-dependent components are

$$(\Delta\boldsymbol{\mathcal{I}})_{13} = \frac{k_2 R^5 \Omega_o^2}{3G}\sin\theta_m\cos\varphi_m\,, \tag{28a}$$
$$(\Delta\boldsymbol{\mathcal{I}})_{23} = \frac{k_2 R^5 \Omega_o^2}{3G}\sin\theta_m\sin\varphi_m\,, \tag{28b}$$

where we have used $\theta_m \ll 1$ to approximate $\cos\theta_m$ by 1. Other components of $\Delta\boldsymbol{\mathcal{I}}$ feature permanent deformation terms and time-dependent terms that are proportional to $\sin^2\theta_m$ which are much smaller in magnitude.

We write the Love number k_2 in terms of a compliance $\mathcal{S}_{11}$ as

$$k_2 = \frac{3G}{R^5\Omega_o^2}\bar{A}\mathcal{S}_{11}\,, \tag{29}$$

where $\bar{A}$ is the mean equatorial moment of inertia. We substitute this relation in Equation (28) and, to add a bit more precision, replace $\bar{A}$ with the appropriate equatorial component of the moment of inertia that is perturbed,

$$(\Delta\boldsymbol{\mathcal{I}})_{13} = B\mathcal{S}_{11}\sin\theta_m\cos\varphi_m\,, \tag{30a}$$
$$(\Delta\boldsymbol{\mathcal{I}})_{23} = A\mathcal{S}_{11}\sin\theta_m\sin\varphi_m\,. \tag{30b}$$

To this, we must add the perturbation in the moment of inertia associated with the misaligned rotation vectors of the fluid and solid cores (by tilt angles θ_f and θ_s, and longitudinal orientations φ_f and φ_s, respectively). Both θ_f and θ_s are small (of the order of a few arcmin or smaller) so their added contribution can be written in the same form as Equation (30),

$$(\Delta\boldsymbol{\mathcal{I}})_{13} = B\Big(\mathcal{S}_{11}\sin\theta_m\cos\varphi_m + \mathcal{S}_{12}\sin\theta_f\cos\varphi_f + \mathcal{S}_{13}\sin\theta_s\cos\varphi_s\Big)\,, \tag{31a}$$

$$(\Delta\boldsymbol{\mathcal{I}})_{23} = A\Big(\mathcal{S}_{11}\sin\theta_m\sin\varphi_m + \mathcal{S}_{12}\sin\theta_f\sin\varphi_f + \mathcal{S}_{13}\sin\theta_s\sin\varphi_s\Big)\,, \tag{31b}$$

where the compliances $\mathcal{S}_{12}$ an $\mathcal{S}_{13}$ capture respectively the global elastic deformations connected with θ_f and θ_s (see Appendix C of MD22).

The compliances $\mathcal{S}_{11}$, $\mathcal{S}_{12}$ and $\mathcal{S}_{13}$ depend on the interior structure and rheology of Mercury. Likewise, the angles θ_m, θ_f and θ_s also depend on the interior structure. Because $\theta_m \ll \theta_f$ (D21) and $\mathcal{S}_{13} \ll \mathcal{S}_{12}$ (MD22), the terms involving $\mathcal{S}_{12}$ are the largest in Equation (31) by at least 2 orders of magnitude: the perturbation in the moment of inertia tensor is dominated by the deformations induced by the precession of the tilted spin axis of the fluid core.

Replacing $\alpha_3\boldsymbol{\mathcal{I}_s}$ with $\Delta\boldsymbol{\mathcal{I}}$ and ΔC_{21}^n by ΔC_{21}^f in the relations of Equation (14) and writing φ_f as in Equation (23) with a deviation of the orientation of the fluid core spin from the Cassini plane by an angle ϕ_f, the time-dependent changes in the Stokes coefficients $\Delta C_{21}^f(t)$ and $\Delta\mathcal{S}_{21}^f(t)$ associated with the precession of the fluid core spin axis are

$$\Delta C_{21}^f(t) = -\Delta C_{21}^f \cos\left(-\Omega_o t + \frac{\pi}{2} - \omega + \phi_f\right)\,, \tag{32a}$$

$$\Delta\mathcal{S}_{21}^f(t) = -\Delta S_{21}^f \sin\left(-\Omega_o t + \frac{\pi}{2} - \omega + \phi_f\right)\,, \tag{32b}$$

where the magnitudes ΔC_{21}^f and ΔS_{21}^f are given by

$$\Delta C_{21}^f = \frac{\mathcal{S}_{12} B}{M_{☿} R^2}\sin\theta_f\,, \tag{33a}$$

$$\Delta S_{21}^f = \frac{\mathcal{S}_{12} A}{M_{☿} R^2}\sin\theta_f\,. \tag{33b}$$

3 Interior structure and rotational model of Mercury

3.1 Interior structure

The amplitude of the degree 2, order 1 gravity signal of internal origin depends on θ_f and θ_n which, in turn, depend on the interior density structure, including the size of the inner core. We use here the model of Mercury's interior density structure and Cassini state presented in D21 and MD22. Mercury is modelled as a simple four layer planet comprised of an inner core, fluid core, mantle and crust, each with a uniform density. The outer spherical mean radii of each of these layers, are denoted by r_s, r_f, r_m, and R, and their densities by ρ_s, ρ_f, ρ_m, and ρ_c, respectively. The inner core radius r_s corresponds to the ICB radius, the fluid core radius r_f to the CMB radius, and R to the planetary radius of Mercury. Neglecting the increase in density with depth due to compressibility is not justified in the core, but adopting uniform densities – representing volume averages – simplifies the analytical expressions of the model. Modifying this interior structure model to take into account variations of density with depth is possible, but the uniform layer model is sufficient for our present purpose, which is to give a first order estimate the amplitude of the gravity signal.

For the crust, we assume a density of $\rho_c = 2974$ kg m^{-3} and a thickness $h = R - r_m =$ 26 km (Sori, 2018). Individual interior models are constructed for each choice of ICB radius, ensuring that they are consistent with $M_☿$ and chosen values of the moments of inertia of the whole planet C and that of the mantle and crust C_m. The latter two are determined from the observed obliquity ε_m and the observed amplitude of 88-day longitudinal librations. We use here the same choices of C and C_m as in D21 and MD22: $C/M_☿R^2 = 0.3455$ and $C_m/M_☿R^2 =$ 0.1475 which were based on the results presented in Margot et al. (2012). Two possible end-member scenarios for how the densities of the solid (ρ_s) and fluid (ρ_f) cores are tied to the size of the inner core were considered in D21. In the first, ρ_s is held constant and ρ_f is adjusted with inner core size (r_s) to match $M_☿$; in the second, it is the density contrast at the ICB which is set to a constant, with both ρ_s and ρ_f modified with r_s. For a given r_s, the solution of the rotational model depends on which scenario is used, but the way the solution changes as a function of r_s is qualitatively similar in either cases. Numerical results are computed here according to the first scenario, with $\rho_s = 8,800$ kg m^{-3}. The amplitude of the gravity signal that we predict with a given choice of r_s does depend on this choice, as they depend on the choice for the crustal density and thickness.

The amplitudes of $\Delta C^n_{21}(t)$ and $\Delta S^n_{21}(t)$ depend on the triaxial shape of the inner core specified in terms of its three principal moments of inertia $C_s > B_s > A_s$. These are built as detailed in D21, that is, with the assumption that both the CMB and ICB are surfaces in hydrostatic equilibrium with the imposed density anomalies originating from the undulating topographies of the surface and crust-mantle interface, and by matching the observed degree 2 Stokes coefficients C_{20} and C_{22}. The numerical values of all parameters are identical to those used in D21 and MD22 and, for convenience, are reproduced in Table 1.

The equatorial moments of inertia A and B, on which the amplitudes $\Delta C^f_{21}(t)$ and $\Delta S^f_{21}(t)$ depend are computed from

$$A = \bar{A} - 2M_☿R^2C_{22}\,, \tag{34a}$$

$$B = \bar{A} + 2M_☿R^2C_{22}\,, \tag{34b}$$

where the mean equatorial moment of inertia $\bar{A}$ is approximated by that for a spherical planet,

$$\bar{A} = \frac{8\pi}{15}\left(\rho_s r_s^5 + \rho_f\left(r_f^5 - r_s^5\right) + \rho_m\left(r_m^5 - r_f^5\right) + \rho_c\left(R^5 - r_m^5\right)\right). \tag{34c}$$

The amplitudes of $\Delta C^{n,f}_{21}(t)$ and $\Delta S^{n,f}_{21}(t)$ also involve the compliance $\mathcal{S}_{12}$ and Love number k_s (which in turn involves the compliance $\mathcal{S}_{14}$). These depend on the choice of a rheology model. The method for their computation is presented in Appendix C of MD22. Of particular note, the rheology is specified such that for each choice of inner core size, the degree 2 Love number k_2 is equal to 0.55, the mean value from the results obtained in two recent studies (Genova et al., 2019; Konopliv et al., 2020). We set the viscosities of the inner core, mantle and crust all equal to 10^{20} Pa s. With this choice, deformations at frequency Ω_o are in the elastic limit,

Mercury Parameter	Numerical value	Reference
mean motion, n	$2\pi/87.96935$ day^{-1}	(Stark, Oberst, & Hussmann, 2015)
rotation rate, $\Omega_o = 1.5n$	$2\pi/58.64623$ day^{-1}	(Stark, Oberst, & Hussmann, 2015)
orbit precession rate, Ω_p	$2\pi/325,513$ yr^{-1}	(Baland et al., 2017)
Poincaré number, $\delta\hat{\omega} = \Omega_p/\Omega_o$	4.9327×10^{-7}	
orbital eccentricity, e_c	0.20563	(Baland et al., 2017)
orbital inclination, I	8.5330°	(Baland et al., 2017)
mean planetary radius, R	2439.360 km	(Perry et al., 2015)
mass, $M_☿$	3.3012×10^{23} kg	(Genova et al., 2019)
mean density, $\bar{\rho}$	5429.5 kg m^{-3}	
J_2	5.0291×10^{-5}	(Genova et al., 2019)
C_{22}	8.0415×10^{-6}	(Genova et al., 2019)
$C/M_☿ R^2$	0.3455	(Margot et al., 2012)
$C_m/M_☿ R^2$	0.1475	(Margot et al., 2012)
polar surface flattening, ϵ_r	6.7436×10^{-4}	(Perry et al., 2015)
equatorial surface flattening, ξ_r	5.1243×10^{-4}	(Perry et al., 2015)

Table 1. Reference parameters for Mercury. The mass $M_☿$ is computed from $GM_☿ = 22031.8636 \times 10^9$ m^3/s^2 taken from Genova et al. (2019). The mean density is calculated from $\frac{4\pi}{3}\bar{\rho}R^3 = M_☿$. The numerical values of ϵ_r and ξ_r are calculated from $\epsilon_r = (\bar{a} - c)/R$ and $\xi_r = (a - b)/R$, where $\bar{a} = \frac{1}{2}(a + b)$ and where $a = 2440.53$ km, $b = 2439.28$ km and $c = 2438.26$ km are the semimajor, intermediate and semiminor axes of the trixial ellipsoidal shape of Mercury taken from Table 2 of Perry et al. (2015). J_2 and C_{22} are computed from Equation (4) in the Supporting Information of Genova et al. (2019).

consistent with our choice of neglecting anelastic contributions to the degree 2, order 1 gravity signal.

3.2 The rotational model

The rotational model that we use to capture the Cassini state of Mercury is described in details in D21 and MD22. The model consists in a linear system of five equations. The five unknowns are the obliquity of the mantle figure ($\tilde{\varepsilon}_m$), the orientations of the rotation vectors of the mantle ($\tilde{m}$), fluid core ($\tilde{m}_f$) and inner core ($\tilde{m}_s$), and the orientation of the inner core figure ($\tilde{n}_s$). Neglecting small amplitude librations, these orientations are fixed when viewed in a frame attached to the Cassini plane. The tilde notation expresses a complex amplitude, with the real and imaginary parts capturing respectively the components that are parallel and orthogonal to the Cassini plane. Viewed in the frame attached to the mantle rotating at sidereal frequency Ω_o, the Cassini plane is rotating in a retrograde direction at frequency $\hat{\omega}\Omega_o$, where $\hat{\omega}$, expressed in cycles per Mercury day, is equal to

$$\hat{\omega} = -1 - \delta\hat{\omega}\cos I\,. \tag{35}$$

The factor $\delta\hat{\omega} = \Omega_p/\Omega_o = 4.933 \times 10^{-7}$ is the Poincaré number, expressing the ratio of the forced precession to sidereal rotation frequencies. [Note that the dimensionless frequency and Poincaré number were denoted by ω and $\delta\omega$, respectively, in D21 and MD22; we use a modified notation here because ω is taken to denote the argument of perihelion, the standard notation in astronomy.] The time-dependent part of the five unknown angles is expressed then by $\exp[i\hat{\omega}\Omega_o t]$. Since $\delta\hat{\omega}$ is very small, the retrograde frequency of the Cassini plane is essentially $-\Omega_o$, equal to the sidereal frequency of Mercury's rotation.

The obliquity ε_m that enters the prediction of $\Delta C_{21}^{ext}(t)$ and $\Delta S_{21}^{ext}(t)$ in Equation (12) is computed from $|\tilde{\varepsilon}_m|$. The tilt angles and longitudinal orientations of the inner core figure (that enter Equation 24) and fluid core spin (Equation 32) are computed from

$$\theta_n = |\tilde{n}_s|\,, \quad \phi_n = \tan^{-1}\left(\frac{\mathrm{Im}[\tilde{n}_s]}{\mathrm{Re}[\tilde{n}_s]}\right)\,, \quad \theta_f = |\tilde{m}_f|\,, \quad \phi_f = \tan^{-1}\left(\frac{\mathrm{Im}[\tilde{m}_f]}{\mathrm{Re}[\tilde{m}_f]}\right)\,. \tag{36}$$

In addition to the pressure and gravitational coupling between the layers, the rotational model also includes viscous and EM coupling the CMB and ICB. As shown in D21, viscous coupling is expected to dominate at the CMB, while EM coupling should dominate at the ICB. We assume an electrically insulating lowermost mantle so that EM coupling at the CMB vanishes. The strength of the viscous torque is set by the choice of a turbulent kinematic viscosity ν assumed equal at both the ICB and CMB. We set the electrical conductivity at 10^6 S m^{-1} in both the solid and fluid cores, and the strength of EM coupling at the ICB is then set by the radial magnetic field strength $\langle B_r\rangle$ threading the boundary. We present results for different choices of ν and $\langle B_r\rangle$.

One important aspect of the model to note is that although the gravitational torque from the Sun is specified in terms of the triaxial shape of Mercury, the angular momentum response to this torque is based on an axisymmetric planet. To first order this is correct as the rotational response of the planet is determined by the resonant amplification of three free modes of rotation (the free precession, the free core nutation and the free inner core nutation) and the latter are quasi-circular motions. This implies that our model predicts an obliquity ε_m and tilt angles θ_n and θ_f that are fixed in time. We must take the triaxiality into account when computing the prediction of the gravity signal of internal origin (and we do, as developed in section 2), but these are computed on the basis of fixed ε_m, θ_n and θ_f.

4 Results

4.1 The degree 2, order 1 gravity signal of internal origin

Figure 2 shows how ε_m, θ_f, θ_n, ϕ_f and ϕ_n vary as a function of inner core size for a fixed kinematic viscosity of $\nu = 10^{-4}$ m^2 s^{-1} and different choices of $\langle B_r \rangle$. For a given inner core size, θ_n (θ_f) increases (decreases) with $\langle B_r \rangle$. The larger $\langle B_r \rangle$ is, the stronger the EM coupling at the ICB is, and the smaller is the misalignment between θ_f and θ_n. The phase angles of the inner core ϕ_n and fluid core ϕ_f with respect to the Cassini plane are respectively negative and positive for a small $\langle B_r \rangle$: the inner core leads ahead of the Cassini plane while the fluid core lags behind it. ϕ_n and ϕ_f are brought closer in alignment with increasing $\langle B_r \rangle$. The inner core and fluid core are locked into a common precession motion when $\langle B_r \rangle$ approaches 1 mT.

The periodic 58.646 day degree 2, order 1 gravity signal from internal origin is the sum of the contributions from the precession of the fluid core spin axis and the precession of the inner core figure (Equations 24 and 32). Figure 3 shows how the magnitudes of the gravity signal from the rigid part ($\Delta C_{21}^{n,rig}$, $\Delta S_{21}^{n,rig}$) and deformation part ($\Delta C_{21}^{n,def}$, $\Delta S_{21}^{n,def}$) associated with the inner core and those associated with the fluid core (ΔC_{21}^{f}, ΔS_{21}^{f}) vary as a function of inner core radius. These are again computed with $\nu = 10^{-4}$ m^2 s^{-1} and for two different choices of $\langle B_r \rangle$, 0.01 mT and 0.3 mT, capturing respectively a weak and strong EM coupling scenarios. Note that the difference between ΔC_{21}^{f} and ΔS_{21}^{f} is very small, indistinguishable in Figure 3. This is because the difference in their magnitudes is proportional to the difference between the maximum (B) and minimum (A) equatorial moments of inertia, which is approximately 1 part in 10^4. In contrast, $\Delta C_{21}^{n,rig}$ and $\Delta S_{21}^{n,rig}$ involve respectively $C_s - A_s$ and $C_s - B_s$. For a triaxial inner core, these deviate substantially from one another: the difference between $\Delta C_{21}^{n,rig}$ and $\Delta S_{21}^{n,rig}$ is of the same order as their individual amplitudes. This is also the case for the deformation part of the inner core signal, $\Delta C_{21}^{n,def}$ and $\Delta S_{21}^{n,def}$, since they are connected to the rigid part by the Love number k_s. Note that k_s is of order 1, and the deformation part is of the same order as the rigid part of the signal.

We also show on Figure 3 how the sum of the magnitudes of the signals from the inner core and fluid core vary with inner core size. These are computed from

$$\Delta C_{21}^{int} = \Delta C_{21}^{f} + \Delta C_{21}^{n,rig} + \Delta C_{21}^{n,def} \,, \tag{37a}$$

$$\Delta S_{21}^{int} = \Delta S_{21}^{f} + \Delta S_{21}^{n,rig} + \Delta S_{21}^{n,def} \,. \tag{37b}$$

ΔC_{21}^{int} and ΔS_{21}^{int} do not represent exactly the amplitudes of the ΔC_{21} and ΔS_{21} gravity signals of internal origin because the contributions from the inner core and fluid core have slightly different phases. Nevertheless, they give a good measure of how their amplitudes change as a function of inner core size. For small inner cores, ΔC_{21}^{int} and ΔS_{21}^{int} are dominated by the contribution from the precession of the fluid core spin axis. Because θ_f decreases with ICB radius, the amplitude of this contribution also decreases with ICB radius. Even though θ_n decreases with ICB radius, the contribution to ΔC_{21}^{int} and ΔS_{21}^{int} from the precession of the inner core increases because the moment of inertia of the inner core increase with ICB radius to the power 5. A stronger EM coupling at the ICB increases θ_n and decreases θ_f, so a larger $\langle B_r \rangle$ enhances the relative contribution of the inner core to ΔC_{21}^{int} and ΔS_{21}^{int}. For a weak EM coupling, the fluid core contribution dominates the gravity signal even for large inner cores. However, for a strong EM coupling, the inner core contribution dominates once the ICB radius exceeds 1000 km.

The greater the relative contribution of the inner core, the larger is the contrast between ΔC_{21}^{int} and ΔS_{21}^{int}. For a strong EM coupling, the minimum inner core radius for which a clear contrast between ΔC_{21}^{int} and ΔS_{21}^{int} emerges is approximately 500 km. For a weak EM coupling, an inner core radius of approximately 1000 km is required. Detecting a difference in the ΔC_{21} and ΔS_{21} signals of internal origin is a diagnostic for the presence of a relatively large, triaxial inner core. The larger the magnetic field at the ICB, the more pronounced the difference is, and the more readily it can be detected.

4.2 Predictions of the time-dependent degree 2, order 1 gravity signal

Figure 4 shows a prediction of the temporal variations of $\Delta C_{21}(t)$ and $\Delta S_{21}(t)$ over four orbital revolutions of Mercury starting from its perihelion position. This prediction includes both the signal from solar tides ($\Delta C_{21}^{ext}(t)$ and $\Delta S_{21}^{ext}(t)$ from Equation 12) and the signal of internal origin from the sum of the contributions from the inner core (Equation 24) and fluid core (Equation 32),

$$\Delta C_{21}^{int}(t) = \Delta C_{21}^{n}(t) + \Delta C_{21}^{f}(t)\,, \tag{38a}$$

$$\Delta S_{21}^{int}(t) = \Delta S_{21}^{n}(t) + \Delta S_{21}^{f}(t)\,. \tag{38b}$$

For the prediction on Figure 4, we have assumed a kinematic viscosity of $\nu = 10^{-4}$ m^2 s^{-1}, an inner core radius of 1000 km and a strong EM coupling scenario with $\langle B_r \rangle = 0.3$ mT. Figure 4 provides an example of the degree 2, order 1 gravity signal that one can expect to observe given a sufficiently good precision.

The external signal includes two dominant periodicities, a prograde 175.94 day signal (or 2 orbital periods) and a retrograde 58.646 day signal (or 2/3 of one orbital period). The temporal variations of the signal is further complicated by the eccentricity of the orbit which modulates the amplitude of the tidal force. The maximum in $\Delta C_{21}^{ext}(t)$ occurs when the combination of small distance to Sun, high solar latitude as seen in Mercury's frame and alignment of the long equatorial axis with the Mercury-Sun line is optimized; this occurs approximately 4.23 days after perihelion. The maximum amplitude of $\Delta S_{21}^{ext}(t)$ is approximately a factor 4 smaller than $\Delta C_{21}^{ext}(t)$.

The signal of internal origin is of similar amplitude as the solar tide signal and comprises only one periodicity, the retrograde 58.646 day period from the precessions of the fluid and solid cores. If both the inner core figure axis and fluid core spin axes were lying in the Cassini plane (i.e. $\phi_n = \phi_f = 0$), the minimum in $\Delta C_{21}^{int}(t)$ shortly after perihelion represents the moment when the Cassini plane is aligned with the meridian of longitude zero. This would occur when $-\Omega_o t + \pi/2 - \omega = 0$, which corresponds to approximately 6.45 days after perihelion. For the

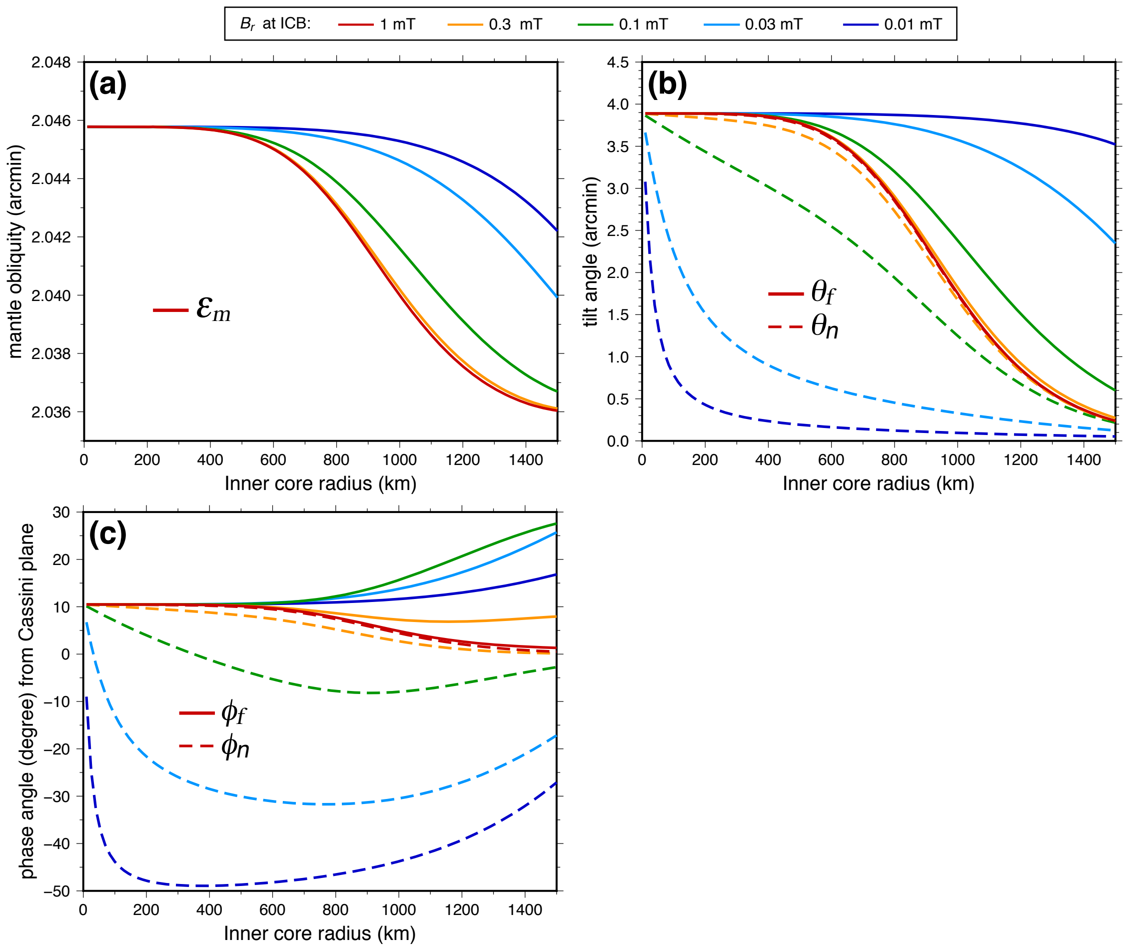

Figure 2. (a) Mantle obliquity (ε_m), (b) tilt angles of the fluid core spin axis (θ_f, solid lines) and inner core figure axis (θ_n, dashed lines) with respect to the mantle, and (c) phase angles of the fluid core spin axis (ϕ_f, solid lines) and inner core figure axis (ϕ_n, dashed lines) with respect to the Cassini plane, as a function of inner core radius and for different choices of magnetic field strength at the ICB (colour in legend).

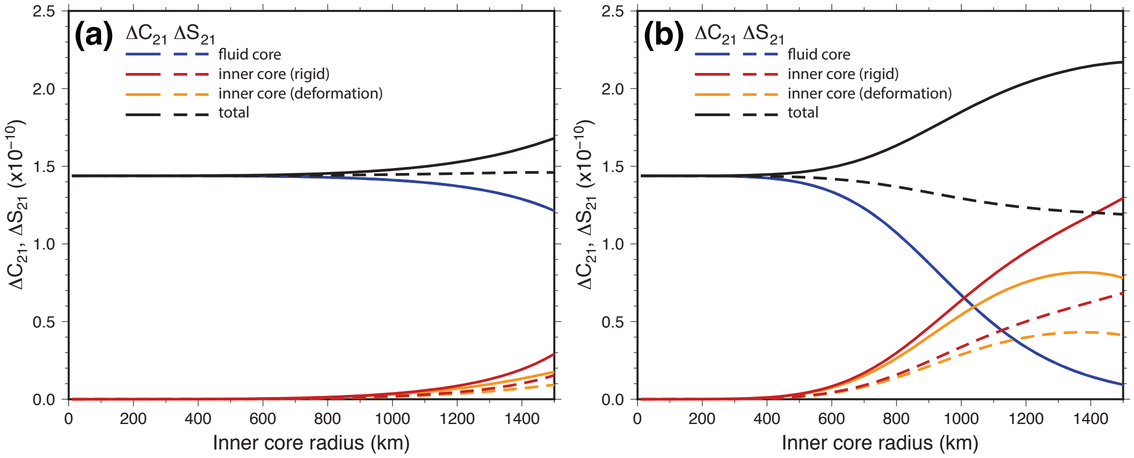

Figure 3. Amplitudes of the ΔC_{21} (solid coloured lines) and ΔS_{21} (dashed coloured lines) periodic 58.646 day gravity signal of internal origin as a function of inner core radius for an assumed magnetic field strength at the ICB of (a) 0.01 mT and (b) 0.3 mT. Shown are the individual contributions from the retrograde precession of the inner core (red), the global elastic deformations induced by the later (orange), the global elastic deformations induced by the retrograde precession of the fluid core spin axis (blue), and their sum (black).

case shown in Figure 4, $\phi_n = 2.64°$ and $\phi_f = 7.21°$, and the minimum in $\Delta C_{21}^{int}(t)$ occurs approximately 7.26 days after perihelion. The internal signal is then approximately in-phase with the 58.646 day solar tide signal, though with a reverse sign.

We denote the difference in the magnitudes of the $\Delta C_{21}^{int}(t)$ and $\Delta S_{21}^{int}(t)$ signals on Figure 4 by

$$\overline{\Delta C_{21}^{int}} = \max\left(\Delta C_{21}^{int}(t)\right) - \max\left(\Delta S_{21}^{int}(t)\right) . \tag{39}$$

As shown above, a non-zero $\overline{\Delta C_{21}^{int}}$ represents a key diagnostic for the presence of a triaxial inner core. Figure 5a shows how $\overline{\Delta C_{21}^{int}}$ changes as a function of inner core size and $\langle B_r \rangle$, for a kinematic viscosity of $\nu = 10^{-4}$ m^2 s^{-1}. The larger the inner core and $\langle B_r \rangle$ are, the greater the contrast between the magnitudes of $\Delta C_{21}^{int}(t)$ and $\Delta S_{21}^{int}(t)$. This contrast becomes discernible (i.e $> 10^{-11}$) for an inner core larger than 500 km for a strong EM coupling at the ICB ($\langle B_r \rangle >$ 0.1 mT). For a weak EM coupling ($\langle B_r \rangle < 0.01$ mT), an inner core radius larger than 1000 km is required. The fluid and solid cores are locked into a common precession motion once $\langle B_r \rangle$ reaches approximately 1 mT; their orientations no longer change for $\langle B_r \rangle > 1$ mT and neither does the profile of $\overline{\Delta C_{21}^{int}}$ versus ICB radius. A specific numerical value of $\overline{\Delta C_{21}^{int}}$ sets a lower bound for the inner core radius, but does not provide a unique determination of its size. As an example, a contrast $\overline{\Delta C_{21}^{int}} = 0.5 \times 10^{-10}$ gives a minimum ICB radius of 950 km assuming a large $\langle B_r \rangle \approx 1$ mT, but a larger ICB radius of 1500 km with a lower $\langle B_r \rangle \approx 0.03$ mT is equally compatible with the same contrast.

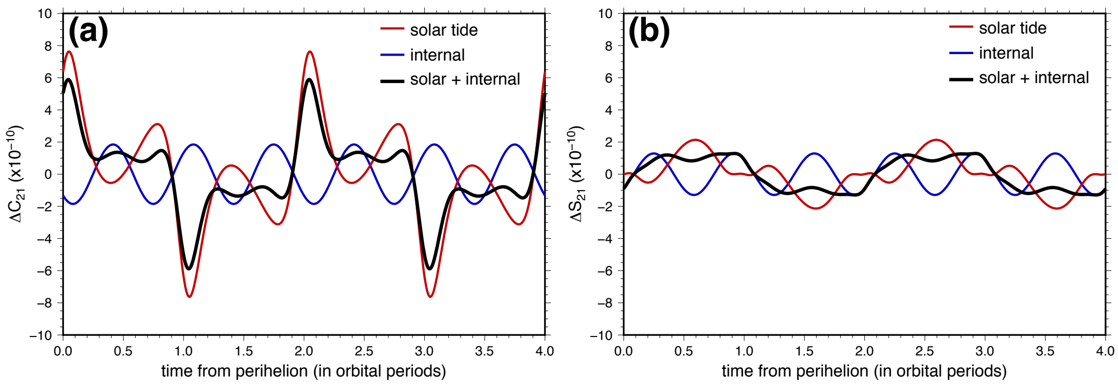

Figure 4. (a) $\Delta C_{21}(t)$ and (b) $\Delta S_{21}(t)$ as a function of time measured in orbital periods of 87.969 days from perihelion. The total signal (black lines) is the sum of the signal produced by solar tides (red) and the signal of internal origin from the retrograde 58.646 day precession of the fluid and solid cores (blue). The latter is based on a inner core radius of 1000 km and a radial magnetic field strength at the ICB of 0.3 mT.

A significant contrast $\overline{\Delta C}_{21}^{int}$ emerges only when $\langle B_r \rangle$ is sufficiently large. This is because a sufficiently strong EM torque on the inner core is required to increase its tilt angle which is otherwise limited due to the strong gravitational coupling with the mantle (D21). A strong EM coupling at the ICB is then a key ingredient to generate an observable $\overline{\Delta C}_{21}^{int}$. Viscous coupling at the ICB and CMB does influence to solution of the Cassini state, but the contrast $\overline{\Delta C}_{21}^{int}$ is much less sensitive to the choice of the kinematic viscosity ν. This is illustrated by Figure 5b, which shows how $\overline{\Delta C}_{21}^{int}$ changes as a function of inner core size and kinematic viscosity, for $\langle B_r \rangle = 0.1$ mT. Hence, while $\overline{\Delta C}_{21}^{int}$ can provide a constraint on $\langle B_r \rangle$, it is largely insensitive to ν.

Different choices of ν and $\langle B_r \rangle$ affect the phases of the $\Delta C_{21}^{int}(t)$ and $\Delta S_{21}^{int}(t)$ signals. In principle then, the phase of these signals can also yield information about the inner core size and coupling at the ICB and CMB. However, we find that the difference in phase compared to a case with no inner core is never more than approximately 1/50th of an orbital period. Such a small phase difference may be difficult to extract from a signal that contains errors. Hence, the difference in the magnitudes of the $\Delta C_{21}^{int}(t)$ and $\Delta S_{21}^{int}(t)$ signals offer a much better prospect of detecting the presence of an inner core than the subtle change in their phases.

5 Discussion and Conclusions

The amplitudes of the 58.646 day periodic $\Delta C_{21}^{int}(t)$ and $\Delta S_{21}^{int}(t)$ signals depend on the size of the inner core, the densities of the fluid and solid cores, the strength of EM coupling at the ICB and the rheology of Mercury. Observing the signal of internal origin can thus provide constraints on Mercury's interior, including its core. In particular, a clear contrast in amplitude between $\Delta C_{21}^{int}(t)$ and $\Delta S_{21}^{int}(t)$ would represent the fingerprint for the presence of a triaxial inner core. The difference in amplitude would not provide a unique measure of inner core

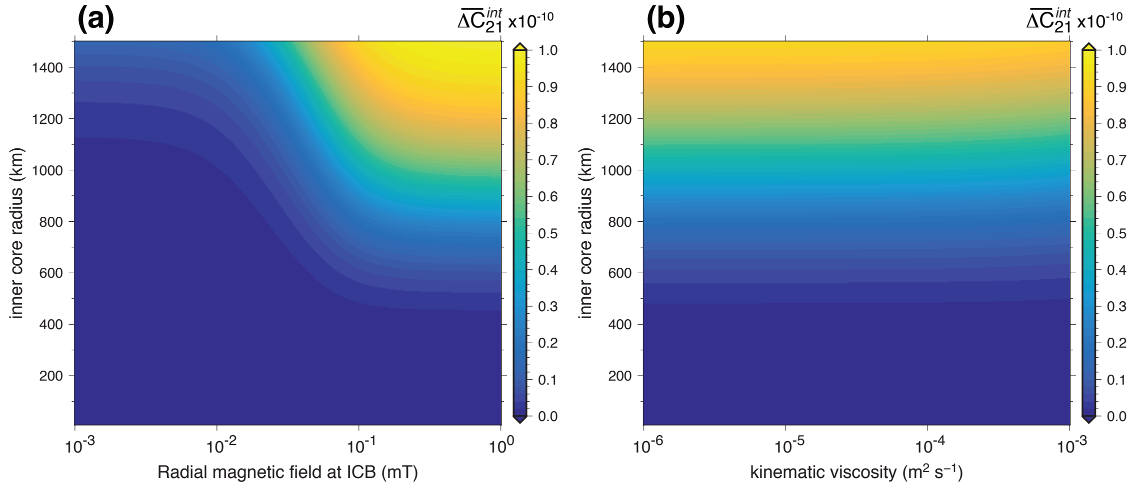

Figure 5. The contrast between the magnitudes of $\Delta C_{21}^{int}(t)$ and $\Delta S_{21}^{int}(t)$ as a function of inner core radius for: (a) different choices of the radial magnetic field at the ICB $\langle B_r \rangle$ and a fixed kinematic viscosity of $\nu = 10^{-4}$ m^2 s^{-1}; and (b) different choices of ν and a fixed $\langle B_r \rangle = 0.1$ mT.

radius, although it would give lower bounds for its size and for the strength of the magnetic field at the ICB.

If the amplitudes of the $\Delta C_{21}^{int}(t)$ and $\Delta S_{21}^{int}(t)$ signals are indistinguishable from one another, it would imply instead a small (< 500 km) or no inner core, and that the signal of internal origin is dominated by elastic deformations induced by the precession of the tilted spin axis of the fluid core. The amplitude of the signal would still provide valuable information on Mercury's interior. Specifically, it would give a measure of the product of the compliance $\mathcal{S}_{12}$ and the tilt angle θ_f, respectively tied to the rheology of Mercury's mantle and the strength of viscous coupling at the CMB.

The largest amplitude contrast between $\Delta C_{21}^{int}(t)$ and $\Delta S_{21}^{int}(t)$ that is predicted by our rotational model (for an inner core radius of 1500 km) is of the order of 10^{-10}. At a co-latitude ϑ and radius r, this corresponds to a difference in gravitational acceleration between a point at longitude zero versus one at a longitude of $\pm 90°$ equal to

$$\Delta g = 3 \frac{GM_{☿}}{r^2} \left(\frac{R}{r} \right)^2 P_{21}(\cos\vartheta)\, \overline{\Delta C}_{21}^{int} \,. \tag{40}$$

At mid-latitude ($\vartheta = 45°$, so then $P_{21}(\cos\vartheta) = 1.5$), and at the surface of Mercury ($r = R$) this gives $\Delta g = 4.5\, g_o \, \overline{\Delta C}_{21}^{int}$ where $g_o = GM_{☿}/R^2 = 3.70$ m s^{-2} is the mean gravitational acceleration. A contrast of $\overline{\Delta C}_{21}^{int} = 10^{-10}$ corresponds to $\Delta g = 1.66 \times 10^{-9}$ m s^{-2} = 166 nGal. At a satellite altitude of approximately 400 km instead of at the surface, $\Delta g = 9.08 \times 10^{-10}$ m s^{-2} = 91 nGal.

These numbers give a sense of the precision in gravity measurements necessary to detect the 58.646 day periodic gravity signal of internal origin. Time-dependent variations in Stokes coefficients of degree 2, order 1 must be resolved with a precision better than 10^{-10}, corresponding to a signal of the order of a few tens of nGal at satellite altitude. The better the precision, the better the prospect of extracting a possible difference between the amplitudes of ΔC_{21}^{int} and ΔS_{21}^{int} and hence to confirm that a solid inner core has nucleated at the centre of Mercury's core.

One of the challenge for the detection of this internal gravity signal is the removal of the tidal gravity signal caused by the Sun. The tidal signal on Mercury is dominated by sectorial tides (degree 2, order 2) and zonal tides (degree 2, order 0), which are respectively 3 and 2 orders of magnitude larger than the tesseral tides (degree 2, order 1) (Van Hoolst & Jacobs, 2003). The main periodicities of the sectorial and zonal tides are 87.969 day (one orbital period) and 43.984 days (1/2 orbital period), so even though they are much larger in magnitude than the tesseral tides, they do not contain power at the sidereal period of 58.646 days. The tidal signal of degree 2, order 1 has main periodicities of 58.646 days and 178.939 days (Van Hoolst & Jacobs, 2003), and as we have shown here, its amplitude is of the same order of magnitude as that induced by the precessing fluid and solid cores. This external signal is known – although it depends on k_2 – so in principle it can be removed from observations to isolate the signal of internal origin.

Observations made by the MESSENGER spacecraft are not sufficiently precise to detect the presence of an inner core through the method that we have presented here. The uncertainties on C_{21} and S_{21} are of the order of 5×10^{-9} (e.g. Table 2 of Konopliv et al., 2020). The upcoming BepiColombo mission should reduce the uncertainties on C_{21} and S_{21} to approximately 5×10^{-10} and 2×10^{-9}, respectively (Milani et al., 2001), approaching but not quite achieving the resolution that is required to detect the periodic signal of internal origin. A future satellite mission, for instance one similar to the GRAIL twin-satellites sent in orbit around the Moon (Zuber et al., 2013), could achieve the desired precision of the order of 10^{-10} or better. An added benefit to such a mission would be an improvement in the precision of k_2 which would permit to remove the solar tide signal more accurately.

Gravity measurements made at a specific location at Mercury's surface by a future lander may also permit a detection of the degree 2, order 1 internal gravity signal. Unlike global gravity observations made by a spacecraft in orbit, measurements at one location at the surface would not give direct information on the contrast between the amplitudes of $\Delta C_{21}^{int}(t)$ and $\Delta S_{21}^{int}(t)$ signals. Instead, a fixed gravimeter would simply measure the gravity signal at that location; $\Delta C_{21}^{int}(t)$ at longitude zero or 180°, $\Delta S_{21}^{int}(t)$ at longitude ±90°. To maximize the amplitude of the degree 2, order 1 signal, the lander should be placed at a latitude of 45° in either hemisphere. As an example, taking an inner core radius of 1100 km, and assuming a ICB magnetic field of 0.3 mT, our model predicts $\Delta C_{21}^{int} \approx 2 \times 10^{-10}$ and $\Delta S_{21}^{int} \approx 1.2 \times 10^{-10}$. At longitude zero the gravity signal would be $\Delta g = 4.5\, g_o \Delta C_{21}^{int} \approx 3.3 \times 10^{-9}$ m s^{-2} = 330 nGal. At longitude ±90°, $\Delta g = 4.5\, g_o \Delta S_{21}^{int} \approx 2.0 \times 10^{-9}$ m s^{-2} = 200 nGal. These amplitudes would be reduced by the radial displacement associated with global elastic deformations.

As noted above, sectorial and zonal tides are much larger than tesseral tides, so the signal recorded by a fixed gravimeter at the surface would be dominated by these. The gravity changes they produce is of the order of 10^{-6} m s^{-2} = 10^5 nGal at a dominant period of 87.969 days (Van Hoolst & Jacobs, 2003; Kudryavtsev, 2008). The predicted tidal signal is modified by the factor $(1 + k_2 - h_2)$. This factor depends on inner core size (Steinbrügge et al., 2018), so extracting it from the observed amplitude of the 88-day gravity signal is another way to reveal the presence of an inner core. In fact, given that a precision of the order of $10^3 – 10^4$ nGal may be required to do so, this may be a better prospect than to try to detect the 100 nGal level of the periodic 58.646 days degree 2, order 1 signal.

The internal gravity signal associated with the precessing fluid and solid cores of Mercury is of the same order of magnitude as that predicted for the Moon (Williams, 2007; Zhang & Dumberry, 2021). While the core of the Moon is small, the tilt angle of its inner core is potentially large because of the resonant amplification due to the proximity of the FICN period with the orbital precession period (e.g. Williams, 2007; Dumberry & Wieczorek, 2016; Stys & Dumberry, 2018). The orbital precession period of Mercury is very long compared to that of its FICN period. Consequently the misalignments of the spin axes of the fluid and solid cores are very small, of the order of a few arcmin (D21). Nevertheless, the internal gravity signal that they induce is of similar amplitude as that for the Moon because Mercury's core is proportionally much larger.

The interior structure model of Mercury that we have used here is sufficient to capture the correct order of magnitude for the gravity signal of internal origin but several improvements can be implemented. This includes taking into account the change of density with depth due to compression in the core. Furthermore, mass anomalies in our interior models are restricted to those caused by the topographies of the external surface and at the interface between interior regions. Allowing for mass anomalies in the deep mantle, either frozen-in or involved in mantle convection, would change the gravitational potential imposed on the core and hence change the amplitude and orientation of the degree 2 topography of the inner core. In turn, this would alter the prediction of the gravity signal associated with its precession.

Detecting the presence of an inner core through the scheme presented here would provide constraints on the thermal evolution of Mercury and that of terrestrial planets and moons in general. It would also provide further information on Mercury's dynamo, not only in constraining the liquid core shell geometry in which it operates, but also on the strength of the magnetic field deep inside the core. A large contrast between the amplitudes of ΔC_{21}^{int} and ΔS_{21}^{int} would indicate a scenario of strong EM coupling at the ICB and a large magnetic field strength of the order of 0.1 mT or larger, three orders of magnitude larger than the field strength at the surface of Mercury which is approximately 300 nT (Anderson et al., 2012; Johnson et al., 2012; Wardinski et al., 2019, 2021). This is possible if Mercury's dynamo field is dominated by small length scales components deep in its interior that are filtered by the skin effect from a thermally stratified layer at the top of the core (Christensen, 2006; Christensen & Wicht, 2008). However, other dynamo scenarios have been proposed for which the internal field is not as strong (e.g. Cao et al., 2014; Tian et al., 2015; Takahashi et al., 2019) and an observation of the gravity signal of internal origin may then help to determine which among these are more plausible.

Acknowledgments

All Figures were created with the GMT software (Wessel et al., 2013). MD is supported by a Discovery Grant from NSERC/CRSNG. The source codes, GMT scripts and data files to reproduce all figures are freely accessible at the following Dataverse repository:

https://doi.org/10.7939/DVN/VVJ97V.

References

Anderson, B. J., Johnson, C. L., Korth, H., Winslow, R. M., Borovsky, J. E., Purucker, M. E., … McNutt, R. L. (2012). Low-degree structure in mercury's planetary magnetic field. *J. Geophys. Res.*, *117*, E00L12. (doi:10.1029/2012JE004159)

Baland, R.-M., Yseboodt, A., M. Rivoldini, & Van Hoolst, T. (2017). Obliquity of Mercury: Influence of the precession of the pericenter and of tides. *Icarus*, *291*, 136–159.

Bertone, S., Mazarico, E., Barker, M. K., Goossens, T. J., S. Sabaka, Neumann, G. A., & Smith, D. E. (2021). Deriving Mercury geodetic parameters with altimetric crossovers from the Mercury Laser Altimeter (MLA). *J. Geophys. Res. Planets*, *126*, e2020JE006683. doi: https://doi.org/10.1029/2020JE006683

Cao, H., Aurnou, J. M., Wicht, J., Dietrich, W., Soderlund, K. M., & Russel, C. T. (2014). A dynamo model explanation for Mercury's anomalous magnetic field. *Geophys. Res. Lett.*, *41*. (doi:10.1002/2014GL060196)

Christensen, U. R. (2006). A deep dynamo generating Mercury's magnetic field. *Nature*, *444*, 1056–1058.

Christensen, U. R., & Wicht, J. (2008). Models of magnetic field generation in partly stable planetary cores: Applications to Mercury and Saturn. *Icarus*, *196*, 16–34.

Colombo, G. (1966). Cassini's second and third laws. *Astron. J.*, *71*, 891–896.

Dumberry, M. (2011). The free librations of Mercury and the size of its inner core. *Geophys. Res. Lett.*, *38*. (L16202, doi:10.1029/2011GL048277)

Dumberry, M. (2021). The influence of a fluid core and a solid inner core on the cassini state of Mercury. *J. Geophys. Res. Planets*, *126*, e2020JE006621.

Dumberry, M., & Rivoldini, A. (2015). Mercury's inner core size and core-crystallization regime. *Icarus*, *248*, 254–268.

Dumberry, M., Rivoldini, A., Van Hoolst, T., & Yseboodt, M. (2013). The role of Mercury's core density structure on its longitudinal librations. *Icarus*, *225*, 62–74.

Dumberry, M., & Wieczorek, M. A. (2016). The forced precession of the Moon's inner core. *J. Geophys. Res. Planets*, *121*, 1264–1292.

Genova, A., Goossens, S., Mazarico, E., Lemoine, F. G., Neumann, G. A., Kuang, W., … Zuber, M. T. (2019). Geodetic evidence that Mercury has a solid inner core. *Geophys. Res. Lett.*, *46*. (doi:10.1029/2018GL081135)

Grott, M., Breuer, D., & Laneuville, M. (2011). Thermo-chemical evolution and global contraction of Mercury. *Earth Planet. Sci. Lett.*, *307*, 135–146.

Guerrero, J. M., Lowman, J. P., & Tackley, P. J. (2021). Did the cessation of convection in Mercury's mantle allow for a dynamo supporting increase increase in heat loss from its core? *Earth Planet. Sci. Lett.*, *571*, 117108.

Hauck, S. A., Margot, J.-L., Solomon, S. C., Phillips, R. J., Johnson, C. L., Lemoine, F. G., … Zuber, M. T. (2013). The curious case of Mercury's internal structure. *J. Geophys. Res.*, *118*. (doi:10.1002/jgre.20091)

Johnson, C. L., Purucker, M. E., Korth, H., Anderson, B. J., Winslow, R. M., Al Asad, M. M. H., … Solomon, S. C. (2012). MESSENGER observations of mercury's magnetic field structure. *J. Geophys. Res.*, *117*, E00L14. (doi:10.1029/2012JE004217)

Knibbe, J. S., Rivoldini, A., Luginbuhl, S. M., Namur, O., Charlier, B., Mezouar, M., … Van Hoolst, T. (2021). Mercury's interior structure constrained by density and P-wave velocity measurements of liquid Fe-Si-C alloys. *Journal of Geophysical Research: Planets*, *126*, e2020JE006651.

Knibbe, J. S., & van Westrenen, S. W. (2015). The interior configuration of planet Mercury constrained by moment of inertia and planetary contraction. *Journal of Geophysical Research: Planets*, *120*. (doi:10.1002/2015JE004908)

Knibbe, J. S., & van Westrenen, S. W. (2018). The thermal evolution of Mercury's Fe-Si core. *EPSL*, *482*, 147–159.

Koning, A. H., & Dumberry, M. (2013). Internal forcing of mercury's long period free librations. *Icarus*, *223*, 40–47.

Konopliv, A. S., Park, R. S., & Ermakov, A. I. (2020). The Mercury gravity field, orientation, love number, and ephemeris from the MESSENGER radiometric tracking data. *Icarus*, *335*, 113386.

Kudryavtsev, S. M. (2008). Harmonic development of tide-generating potential of terrestrial planets. *Celest. Mech. Dyn. Astr.*, *101*, 337–348.

MacPherson, I., & Dumberry, M. (2022). Deviation of Mercury's spin axis from an exact Cassini state induced by dissipation. *J. Geophys. Res. Planets*. (preprint available at: https://www.essoar.org/doi/10.1002/essoar.10510041.2)

Margot, J. L., Peale, S. J., Jurgens, R. F., Slade, M. A., & Holin, I. V. (2007). Large longitude libration of Mercury reveals a molten core. *Science*, *316*, 710–714.

Margot, J. L., Peale, S. J., Solomon, S. C., Hauck, S. A., Ghigo, F. D., Jurgens, R. F., ... Campbell, D. B. (2012). Mercury's moment of inertia from spin and gravity data. *J. Geophys. Res.*, *117*, E00L09. (doi:10.1029/2012JE004161)

Milani, A., Rossi, A., Vokrouhlický, D., Villani, D., & Bonanno, C. (2001). Gravity field and rotation state of Mercury from the BepiColombo Radio Science Experiments. *Planetary and Space Science*, *49*, 1579–1596.

Murray, C. D., & Dermott, S. F. (1999). *Solar System Dynamics.* New Yok, USA: Cambridge University Press.

Peale, S. J. (1969). Generalized Cassini's laws. *Astron. J.*, *74*, 483–489.

Peale, S. J., Margot, J. L., Hauck II, S. A., & Solomon, S. C. (2014). Effect of core-mantle and tidal torques on Mercury's spin axis orientation. *Icarus*, *231*, 206–220.

Peale, S. J., Margot, J. L., Hauck II, S. A., & Solomon, S. C. (2016). Consequences of a solid inner core on Mercury's spin configuration. *Icarus*, *264*, 443–455.

Peale, S. J., Phillips, R., Solomon, S., Smith, D., & Zuber, M. (2002). A procedure for determining the nature of Mercury's core. *Meteor. Planet. Sci.*, *37*, 1269–1283.

Perry, M. E., Neumann, G. A., Phillips, R. J., & et al. (2015). The low-degree shape of Mercury. *Geophys. Res. Lett.*, *42*, 6951–6958.

Sori, M. M. (2018). A thin, dense crust for Mercury. *Earth Planet. Sci. Lett.*, *489*, 92–99.

Stark, A., Oberst, J., & Hussmann, H. (2015). Mercury's resonant rotation from secular orbital elements. *Celest. Mech. Dyn. Astr.*, *123*, 263–277.

Stark, A., Oberst, J., Preusker, F., Peale, S. J., Margot, J.-L., Phillips, R. J., ... Solomon, S. C. (2015). First MESSENGER orbital observations of Mercury's librations. *Geophys. Res. Lett.*, *42*, 7881–7889.

Steinbrügge, G., Dumberry, M., Rivoldini, A., Schubert, G., Cao, H., Schroeder, D. M., & Soderlund, K. M. (2021). Challenges on Mercury's interior structure posed by the new measurements of its obliquity and tides. *Geophys. Res. Lett.*, *48*, e2020GL089895. doi: https://doi.org/10.1029/2020GL089895

Steinbrügge, G., Padovan, S., Hussmann, H., Steinke, T., Stark, A., & Oberst, J. (2018). Viscoelastic tides of Mercury and the determination of its inner core size. *Journal of*

Geophysical Research: Planets, *123*, 2760–2772. (doi:10.1029/2018JE005569)

Stys, C., & Dumberry, M. (2018). The cassini state of the Moon's inner core. *J. Geophys. Res. Planets*, *123*, 1–25. (doi:10.1029/2018JE005607)

Takahashi, F., Shimizu, H., & Tsunakawa, H. (2019). Mercury's anomalous magnetic field caused by a symmetry-breaking self-regulating dynamo. *Nature Communication*, *10*, 208. (https://doi.org/10.1038/s41467-018-08213-7)

Tian, Z., Zuber, M. T., & Stanley, S. (2015). Magnetic field modeling of Mercury using dynamo models with a stable layer and laterally variable heat flux. *Icarus*, *260*, 263–268.

Tosi, N., Grott, M., Plesa, A.-C., & Breuer, D. (2013). Thermochemical evolution of Mercury's interior. *J. Geophys. Res.*, *118*, 1–14. (doi:10.1002/jgre.20168)

Van Hoolst, T., & Jacobs, C. (2003). Mercury's tides and interior structure. *J. Geophys. Res.*, *108*, 5121. (doi:10.1029/2003JE002126)

Van Hoolst, T., Rivoldini, A., Baland, R.-M., & Yseboodt, M. (2012). The effects of tides and an inner core on the forced libration of mercury. *Earth Planet. Sci. Lett.*, *333–334*, 83–90.

Veasey, M., & Dumberry, M. (2011). The influence of Mercury's inner core on its physical libration. *Icarus*, *214*, 265–274.

Wardinski, I., Amit, H., Langlais, B., & Thébault, E. (2021). The internal structure of Mercury's core inferred from magnetic observations. *Journal of Geophyisical Research: Planets*, *126*, e2020JE006792.

Wardinski, I., Langlais, B., & Thébault, E. (2019). Correlated time-varying magnetic fields and the core size of Mercury. *Journal of Geophyisical Research: Planets*, *124*, 2178–2197.

Wessel, P., Smith, W. H. F., Scharroo, R., Luis, J., & Wobbe, F. (2013). Generic Mapping Tools: Improved version released. *EOS Trans. AGU*, *94*, 409–410.

Williams, J. G. (2007). A scheme for lunar inner core detection. *Geophys. Res. Lett.*, *34*, L03202. (doi:10.1029/2006GL028185)

Williams, J. G., Konopliv, A. S., Park, R. S., Yuan, D.-N., Asmar, S. W., Watkins, D. E., … Zuber, M. T. (2015). The deep lunar interior from GRAIL. In *46th lunar and planetary science conference, the woodlands, tx, march 16-20.* (abstract #1380)

Yseboodt, M., Rivoldini, A., Van Hoolst, T., & Dumberry, M. (2013). Influence of an inner core on the long period forced librations of Mercury. *Icarus*, *226*, 41–51.

Zhang, J., & Dumberry, M. (2021). Viscous dissipation in the fluid core of the Moon. *J. Geophys. Res. Planets*, *126*, e2021JE006966. doi: 10.1029/e2021JE006966

Zuber, M. T., Smith, D. E., Watkins, M. M., Asmar, S. W., Konopliv, A. S., Lemoine, F. G., … Yuan, D.-N. (2013). Gravity field of the Moon from the Gravity Recovery and Interior Laboratory (GRAIL) Mission. *Science*, *339*(6120), 668–671. doi: 10.1126/science.1231507